Correspondence to:
Z. Dai,
zjdai@sklec.ecnu.edu.cn

Detection of Linkage Between Solar and Lunar Cycles and Runoff of the World's Large Rivers

Zhijun Dai[1,2] [ID], Jinzhou Du[1] [ID], Zhenghong Tang[3], Suying Ou[4], Samuel Brody[5], Xuefei Mei[1], Jietai Jing[6], and Shoubing Yu[7]

[1]State Key Laboratory of Estuarine and Coastal Research, East China Normal University, Shanghai, China, [2]Key laboratory of Environment Change and Resources Use in Beibu Gulf, Ministry of Education, Nanning Normal University, Nanning, China, [3]Community and Regional Planning Program, University of Nebraska-Lincoln, Lincoln, NE, USA, [4]Institute of Estuarine and Coastal Research, Sun Yat-sen University, Guangzhou, China, [5]Center for Texas Beaches and Shores, Texas A&M University, Galveston, TX, USA, [6]State Key Laboratory of Precision Spectroscopy, Department of Physics, East China Normal University, Shanghai, China, [7]Yellow River Institute of Hydraulic Research, Yellow River Conservancy Commission, Zhengzhou, China

Abstract It is an ongoing concern that global hydrological cycle can be likely intensified under context of climate change and anthropogenic actions. Here, our results show that the solar and lunar periodic motions (SLPMs) have substantial impact on the runoff of the world's large rivers. We estimate that SLPMs can produce a change of the world's large rivers runoff by as much as 6.7%. Although climate models suggest that the increased frequency of extreme events is attributed to anthropogenic activities, it is out of our expectation that as much as 73% and 85% of the extreme flood and drought events (based on runoff discharged to the ocean) appear in resonance with SLPMs, respectively. A reevaluation of impacts of SLPMs on changes in the world's river runoff is urgently needed, especially when extreme drought and flood events are on the rise.

1. Introduction

Solar and lunar periodic motions (SLPMs) are significant factors that affect the Earth's surface processes (Scafetta, 2013). As the Sun is the primary source of energy for the Earth's climate system, its magnetic cycles of about 11 years play a key role in the variability of the Earth's climate (Gray, 2003; Intergovernmental Panel on Climate Change, IPCC, 2007; Rind, 2002). Moreover, it has been found that the 18.6-year cycle due to the precession of the Moon's nodes has a key impact on climate (Camuffo, 2001). However, climate models show that anthropogenic activities have increasing influence on the characteristics of rivers when compared with natural variability. The impacts of SLPMs on global runoff changes are gradually becoming less evident with increased human activities (IPCC, 2007; North & Stevens, 1998). Although SLPMs produce a weak modulation on the Earth's albedo, this can easily result in climatic amplification effects (Camuffo, 2001; Scafetta, 2013).

Runoff is important and necessary for human and natural development. Due to the complex nature of climate changes and of anthropogenic forcing (Allen & Ingram, 2002; Lu, 2004; Mei et al., 2018; Tang & Lettenmaier, 2012; Zhang et al., 2010, 2011), the future variability of runoff is unpredictable. Although there are data that show an increase in runoff as a result of upward trends in precipitations (Chou, 2013), a few of the studies have found that runoff changes could also be related to SLPMs (Antico & Kröhling, 2011; Cerveny et al., 2010; Mauas et al., 2008). Specifically, Cerveny et al. (2010) showed the lunar tidal influence on inland rivers at a monthly scale through precipitation. Briciu (2014) furtherly discovered that Moon has semidiurnal tidal influence on no-tidal inland rivers in the United States, Honduras, and Australia. Meanwhile, Lindsay and Farnsworth (1997) indicated solar radiation impaction on streamflow by daily potential evaporation. Lei et al. (2014) documented that solar radiation account for 14% of the overall increase in annual runoff of the Haihe River in China. Hajian and Movahed (2010) investigated that there are some crossovers in the cross-correlation fluctuation function versus timescale of the selected river flow in the United States and sunspot series. Mauas et al. (2008) found a strong correlation between sunspot number and streamflow in South American river. In addition, several studies reveal that solar activities have potential impacts on streamflow extremes, such as flood events (Prokoph et al., 2012; Timoney et al., 1997). However, the present studies about SLPMs impacts on hydrological processes were limited to regional rivers with significant local features (Alexander & Emeritus, 2005; Antico & Kröhling, 2011; Briciu, 2014;
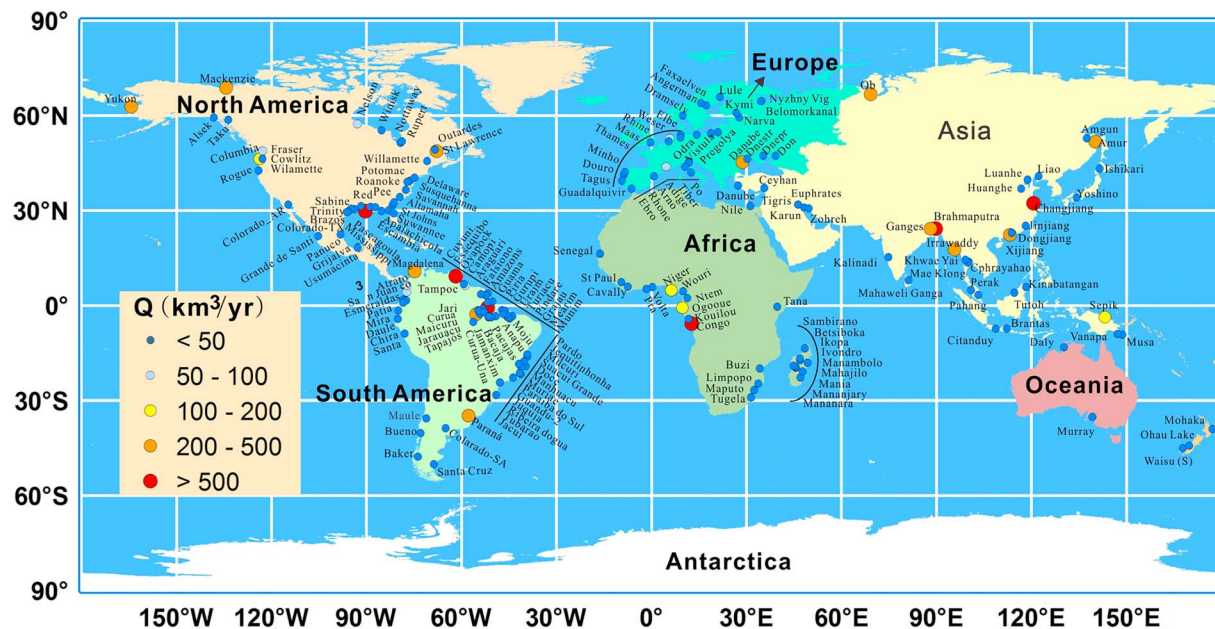
Figure 1. Hydrological stations at the 219 world's largest rivers with annual discharges exceeding 2 km^3/year. Labeled rivers are typical of the world's largest rivers.

Seleshi et al., 1994). No study has attempted to quantitatively estimate the contributions of SLPMs to global runoff changes and especially to extreme drought and flood events. Here, we aim to examine the linkage between global runoff variability and SLPMs and thus estimate the impacts of SLPMs on rivers, extreme drought, and flooding worldwide.

2. Data and Methods

2.1. Data Collection

Recently, Dai and Trenberth (2002) merged data archived from the National Center for Atmospheric Research (http://rda.ucar.edu), the Global Runoff Data Centre (http://grdc.bafg.de), and the University of New Hampshire (http://www.r-arcticnet.sr.unh.edu) to create a new global data set that contains monthly runoff information from the farthest downstream stations for the world's 925 largest ocean-reaching rivers (http://www.cgd.ucar.edu/cas/adai/data-dai.html). In this new global runoff data set, the runoff data for the period 1948–2004 are fairly complete, which is more reliable for assessments of decadal and long-term changes in continental freshwater discharge into the oceans (Dai et al., 2009). Meanwhile, according to Random sampling of Nyquist, the sample rate frequency should be greater than twice the highest-frequency component of interest in the measured signal (Mishali & Eldar, 2010). Thereafter, the used runoff data length from 1948 to 2004 (56 years) can match the requirement to study fluctuation periods of 8.5–12 and 17–21.5 years, which covers as least three cycles of the 18-year period. In the present work, 190 large global rivers were selected (http://www.cgd.ucar.edu/cas/adai/data-dai.html) by considering rivers with annual runoffs of over 2 km^3/year (Figure 1; Appendix A). The selected 190 rivers cover environments ranging from tropical to high-altitude locations. The locations of the observation stations range from 50.25°S to 68.75°N latitude and from −164.25°W to 177.13°E longitude, drainage areas ranging from approximately 580 to $4,620 \times 10^3$ km^2. To ensure the validity of the calculated results, the monthly discharge data in the period 1879–2010 from U.S. Geological Survey (http://waterdata.usgs.gov/nwis) for the Columbia River were selected for comparison with the data from Dai and Trenberth (2002).

Moreover, the recurrence years of crests and troughs for the solar cycles over ~11 years refer to those with periods of maximum and minimum sunspot counts, respectively. The recurrence years of the crests and troughs of the lunar cycles over ~18.6 years corresponded to those with a maximum lunar declination of 28°36′ and a minimum lunar declination angle of 18°20′ between the Moon's orbit and Earth's equator. The crests and troughs of the solar cycles can be calculated based on the number of sunspots from 1948 to

2004, which is obtained from the National Aeronautics and Space Administration, USA (http://solarscience. msfc.nasa.gov). To this end, the crests and troughs of the lunar cycles can be obtained from the lunar declination values given by the National Aeronautics and Space Administration Jet Propulsion Laboratory (http://ssd.jpl.nasa.gov/?horizons).

2.2. Methods

Wavelet analysis (WA) has been widely applied in studies of hydrological processes in recent decades (Brillinger, 1994; Coulibaly & Burn, 2004). It consists of several mathematical transforms through which a temporal (or spatial) series can be transformed into a two-dimensional time and space frequency representation (Mount et al., 2013). The advantage of WA is that the procedure can offer fine time resolution for long-duration signals and frequency resolution for high-frequency signals. The multiresolution decomposition enables the division of data, functions, or operators into various scale components. Each component can then be investigated with a resolution that matches its scale (Hsu & Li, 2010). Because the normalized runoff time series has high-frequency components for short durations and low-frequency components for long durations, WA is well suited to research multiscale and nonstationary runoff properties over finite spatial and temporal domains.

A detailed treatment of the mathematics of WA has been described in previous research (Sadowsky, 1996; Torrence & Compo, 1998). The following is our procedure for data analysis:

Deconstruct the time series of normalized runoff into different fluctuations.

1. Here, the continuous wavelet transform of a time domain function $f(t)$ in relation to a base function (wavelet) $\psi(t)$ can be expressed as follows:

$$W(s, \tau) = \frac{1}{\sqrt{s}} \int_{-\infty}^{\infty} \psi^* \left(\frac{t-\tau}{s} \right) f(t) \mathrm{d}t \tag{1}$$

where ψ^* is the complex conjugate of ψ, s, and τ are the translation (shift) and timescale (dilation) parameters, respectively. $f(t)$ refers to the normalized runoff of each river, and W refers to the corresponding wavelet coefficient of $f(t)$, which is a function of the time and scale of each wavelet. s is determined by the following two formulas:

$$s_j = s_0 2^{(j-1)\delta j} j = 1, 2, ... J \quad J = \delta_j^{-1} \log_2 \left({N\delta_t}/{s_0} \right) $$

where δ_t is the sampling time interval. In this study, δ_t is 1 month, and $s_0 = 2\delta_t, \delta_j = 0.125$.

Many wavelets (e.g., the Mexican hat wavelet, Haar wavelet, and Morlet wavelet) are widely used in time domain transformations (Mallat, 1989). Complex wavelets, such as Morlet wavelets, are more appropriate than other wavelets in the analysis of periodic or characteristic scales in a time series (Hsu & Li, 2010; Kumar & Foufoula-Georgiou, 1997). Therefore, a normalized runoff time series can be transformed based on the Morlet wavelet. The Morlet wavelet can be written as

$$\psi(t) = \pi^{-1/4} e^{i\omega_0 t} e^{-t^2/2} \tag{2}$$

where π is the circular frequency and ω_0 is a nondimensional constant that permits an exchange between time and frequency resolutions. ω_0 has been commonly set at 0.6 in previous studies (Torrence & Compo, 1998).

With respect to the Morlet wavelet, the transform timescale (s) corresponds to period (T) of the Fourier analysis is as follows:

$$T = \frac{4\pi s}{\omega_0 + \sqrt{2 + \omega_0^2}} \tag{3}$$

2. Reconstruct the time series of the normalized runoff into the selected fluctuations.

When the normalized runoff time series is transformed through the Morlet wavelet, the selected fluctuations (j_1 to j_2) in the different timescales can be reconstructed as follows Torrence and Compo (1998):

$$x_n{'} = \frac{\delta_j \delta_t^{1/2}}{C_\delta \psi_0(0) \sum\limits_{j_1}^{j_2} \frac{(W'(s,\tau))}{s_j^{1/2}}} \tag{4}$$

where x_n' is the reconstructed time series, δ_j is the determined spatial resolution of the wavelet spectrum, and C_δ is a constant of the reconstructed time series. Here, for the periodic changes of solar motion, j_1 and j_2, are 8.5 and 12 years, respectively; for the periodic changes of lunar motion, j_1 and j_2, are 17.5 and 21.5 years, respectively.

3. The cone of influence and global wavelet spectrum.

To clearly diagnose the different oscillations of the runoff series, the global wavelet spectrum is utilized to determine the periodic characteristics of all rivers runoff time series. Percival (1995) showed that the global wavelet spectrum provides an unbiased and consistent estimation of the true power spectrum of a time series compared to Fourier spectrum analysis. More detailed definitions and calculations of the global wavelet spectrum can be found in previous reports (Lindsay et al., 1996; Percival, 1995). It can be represented as follows:

$$\overline{W}^2(s) = \frac{1}{N} \sum_{n=0}^{N-1} |W_n(s)|^2 \tag{5}$$

where N is the length of time series. Moreover, red noise wavelet power spectra were used to check the significance ($p < 0.05$) of a peak in the global wavelet spectrum of the runoff of each river, as described by Torrence and Compo (1998). Because a finite-length time series is being considered, errors will occur at the beginning and end of the wavelet power spectrum. However, padding the spectrum with zeroes will introduce discontinuities at the endpoints. Therefore, the cone of influence, where edge effects of wavelet spectrum are important, indicates the *e*-folding time for wavelet power's autocorrelation at each scale (Torrence & Compo, 1998). The calculation program is available from the website (http://paos.colorado.edu/research/wavelets/).

Based on each transform timescale (s), a corresponding T can be obtained for the normalized monthly runoff of 190 rivers (with annual runoffs over 2 km^3/year) at the significance level of 0.05. The signal intensity of seasonal and annual oscillations in river runoff is much larger than those of the relatively long oscillations in global wavelet spectrum, which can cause the relatively long period fail to pass the statistical test (Figures 2a–2f). Therefore, in order to eliminate the effects of periods below 2-year, seasonal and annual oscillations in all riverine runoffs were filtered first, and then the remnant components were reconstructed and can be transformed by the Morlet wavelet method again. The reconstructed time series has a mean square error of less than 1% with robust testing at a significance level of 0.001, which indicates that the decomposition technique is valid. It can be clearly seen that the relatively long periods pass the statistical test when seasonal fluctuations were filtered from the river runoff series.

Furtherly, the reconstructed time series, including fluctuation periods greater than and less than 10 years, were assumed to show the low- and high-frequency fluctuations, which can be used to diagnose the impact of different factors on changes in runoff. In the reconstructed time series, fluctuation periods of 8.5–12 and 17–21.5 years were directly linked to impacts of ~11 years of solar cycles associated with magnetic fields, and impacts of ~18.6 years of lunar cycles related to lunar orbits, respectively (Antico & Kröhling, 2011; Currie & Vines, 1996).

4. Variance contribution of different fluctuations to the entire normalized river runoffs.

The variance of a random sample is calculated by the following formula:

$$S^2 = \frac{\sum_{i=1}^{n}(x_i - \overline{x})^2}{n-1} \tag{6}$$

where S^2 is sample variance, $x_1, x_2, \dots, x_n$ is the sample data set, x is mean value, and n is the size of the data
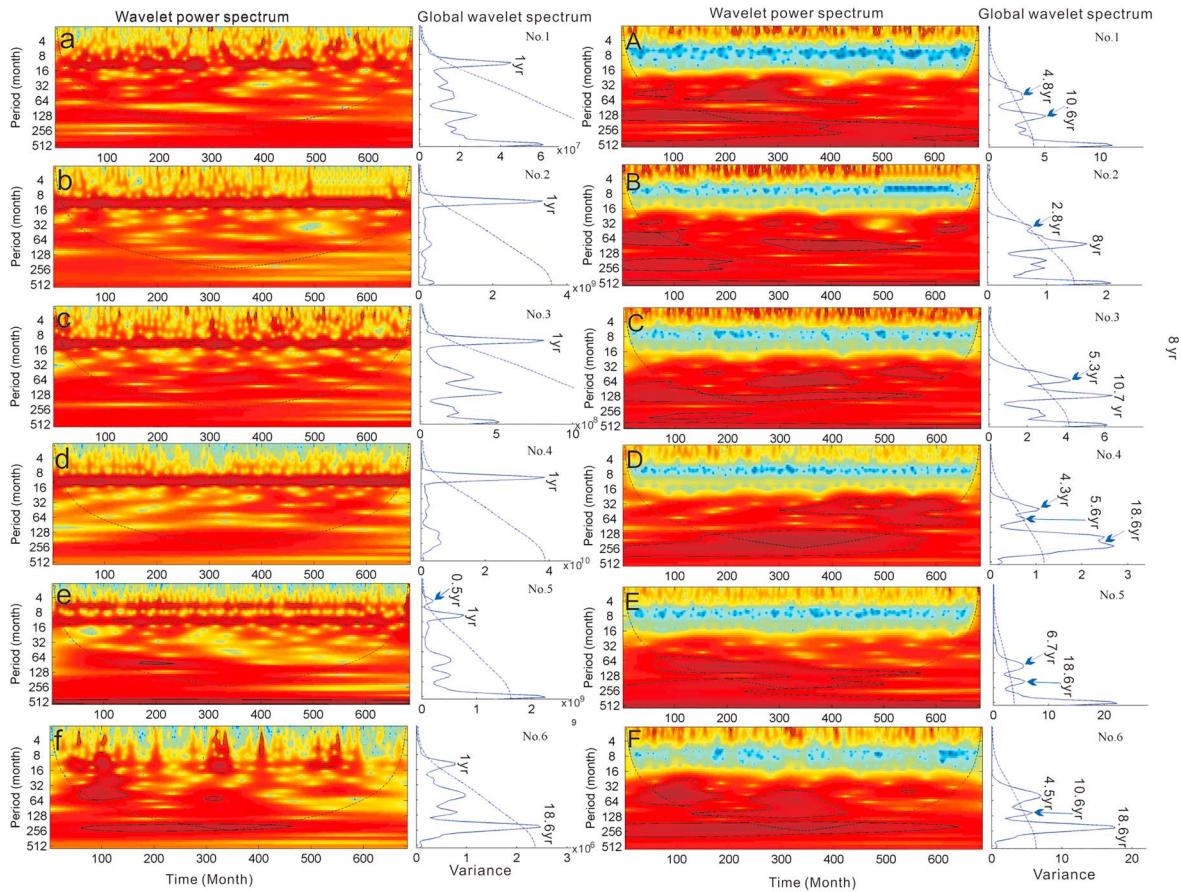
Figure 2. Examples of the fluctuations of the normalized runoff of the world's rivers based on Morlet wavelet analysis and global wavelet spectra. The region under the black cone curve represents the "cone of influence." The thick black contour encloses regions of greater than 95% confidence for a red noise process and with a lag-1 coefficient of 0.72. Both the thick dashed lines and blue curve of the period-variance plot show the 95% confidence level for the red noise spectrum and the global power spectrum, respectively. Nos. 1–6, named as the European Danube (No. 1), the Asian Changjiang (No. 2), the North American Mississippi (No. 3), the South American Amazon (No. 4), the African Niger (No. 5), and the Australian Murray (No. 6) rivers, are designated as representative of the 190 river normalized discharge time series. The left panels (a–f) show the decomposed results from a Morlet wavelet analysis based on the normalized runoff time series, and the right panels (A–F) show the decomposed results from a Morlet wavelet analysis based on the normalized runoff time series with filtered quasi-year fluctuations.

set. Variances of three type of data series, namely, reconstructed time series with fluctuation periods of 8.5–12 years (solar effect), reconstructed time series with fluctuation periods of 17–21.5 years (lunar effect), and the original normalized river discharge series for the 190 rivers are calculated first. The variances of solar and lunar effect series are then respectively divided by the variance of the original series for each river. The obtained two ratios are respectively indication of the effects of solar motion and lunar motion on the river runoff for each river. Their mean values for the 190 rivers therefore are used to represent the contribution of solar and lunar cycles on global river discharge.

5. Correlation of years of SLPM crests and troughs with years of extreme drought and flood.

First, to determine whether there is a statistically significant relationship between the changes in the number of sunspots and the reconstructed discharge over an 11-year cycle, representative rivers of six continents were selected to analyze any possible phase changes corresponding to changes in the number of sunspots using regression analysis. Second, to calculate the number of occurrences of extreme drought and floods in the basins of the 190 largest rivers in the world, we followed the definition of extreme events at percentiles of both P90 and P10 (IPCC, 2007), and in addition, used P95 and P5 to define extreme flood and extreme drought, respectively. When the runoff value in a year was over/below the value of P95/P5, one occurrence of flood or drought was counted. Thus, the number of occurrences of extreme floods and droughts for each river during the observation period can be determined.

AGU
100
ADVANCING EARTH
AND SPACE SCIENCE

Earth and Space Science

10.1029/2018EA000541

Finally, in order to obtain the corresponding years coinciding with the crests and troughs of the fluctuation periods of 8.5–12 and 17–21.5 years in river runoffs, a second order differential equation was used for the reconstructed time series of 8.5–12 and 17–21.5 years. The second differential is a measurement to illustrate how the rate of a quantity change is changing. For the graph of one function, the second differential corresponds to the curvature or concavity of the graph. The positive second differential curve in this graph is upward while the negative second differential curves are downward. Therefore, all years in which the crests and troughs of the fluctuation periods of 8.5–12 and 17–21.5 years occurred in conjunction with extreme drought and floods can be counted.

3. Results

3.1. Periodic Fluctuations of Rivers Runoff

Our WA and the global wavelet spectrum demonstrate that periodic behavior of the 190 rivers is statistically significant. It was determined that variations in runoff of the six representative rivers selected from six continents can be considered representative of the 190 rivers (Figure 2) and only indicate quasi 2-year oscillations as statistically significant (Figures 2a–2f). In spite of the occurrence of periodic oscillations over 10 years, the selected rivers fail to pass the red noise test under the cover of 2-year oscillations (Figures 2a–2f). When oscillations below 2 years were filtered, the behavior of the relatively long oscillations with frequency fluctuations of approximately 4–7, 8–12, and 17–21 years can be clearly seen in Figure 2 (Figure 2A–2F). There was no significant change in the runoff periodic fluctuations longer than 10 years even if anthropogenic activities (i.e., dams) produced decreased tendencies for annual runoff for some rivers, such as the Mississippi, Danube, Changjiang, and Huanghe (Dai et al., 2014; Milliman et al., 2008; (Figures 2A–2C). However, the strong quasi 2-year oscillations in the Murray River experienced intermittently interruptions, when compared to those of the Changjiang, Amazon, etc. (Figures 2a, 2d, and 2f), due to the operation of the Snowy Mountains Hydro-Electric Scheme. Similar interruptions have also been observed in the case of the Colorado River (White et al., 2005). This phenomenon implies that runoff changes at a monthly or annual scale could be affected by regional human activities (Labat et al., 2004; White et al., 2005).

Moreover, when considering the variance contributions of the periodic cycles over 8.5–12 and 17.5–21.5 years, it is noteworthy that variance contributions of the periodic cycles longer than 10 years for each river can represent the 10% to 78% of all runoffs, with a mean of 26%, which accounts for approximately one fourth of the total runoff in the global 190 large rivers (supporting information Table S1). These results indicate that there is a substantial contribution to runoff changes in global rivers over 10-year cycles. In addition, we found that the contribution of SLPMs to the variation of the runoff of all of the rivers ranges from 0.02% to 13.87% for solar effects, with an average 4.32%, and ranges from 0.03% to 8.0% for lunar effects, with an average of 2.35% (supporting information Table S1). The average 2.35% contribution for lunar effects is comparable to that of the tidal amplitude produced by the 18.6-year nodal tidal cycle (Gratiot, 2007). Meanwhile, it can be found that the mean contribution of SLPMs to the 190 river runoff is as high as 6.7% (supporting information Table S1).

When considering the six continents included in this study, the variance contributions of solar and lunar motions to runoff variations of the 190 rivers are presented in Figure 3. The mean contributions of both solar and lunar effects on runoff in Australia are the largest, with over 7.8%, followed by Africa as the second largest, while Europe indicates the smallest value with approximately 5.89% (Figure 3). Our results also indicate that SLPMs have notable latitude zone effects on runoff changes (Figure 3). There are decreasing rates of SLPMs contribution to runoff from the Equator to the polar zones (Figures 3a and 3b). For example, runoffs for the rivers located in the equatorial zone, including the Amazon and the Piria in the South American, the Wouri in the Africa, and the Musa in the Oceania, mainly indicate high contribution values of over 8.5% (Figure 3). However, the effects of SLPMs on rivers located at latitudes above 60°N or 60°S, such as the Lule, Nyzhny Vig, and Ob Rivers, are less than 4% (Figure 3). Moreover, two areas that have high SLPMs contribution rates are located near the equator and in the midlatitude regions (Figure 3) and include Africa, Oceania, and Europe; inversely, relatively low contribution rates are associated with areas mainly located in the subtropical and polar zones, such as parts of Asia, Europe, and North America.

AGU
100
ADVANCING EARTH
AND SPACE SCIENCE

Earth and Space Science

10.1029/2018EA000541
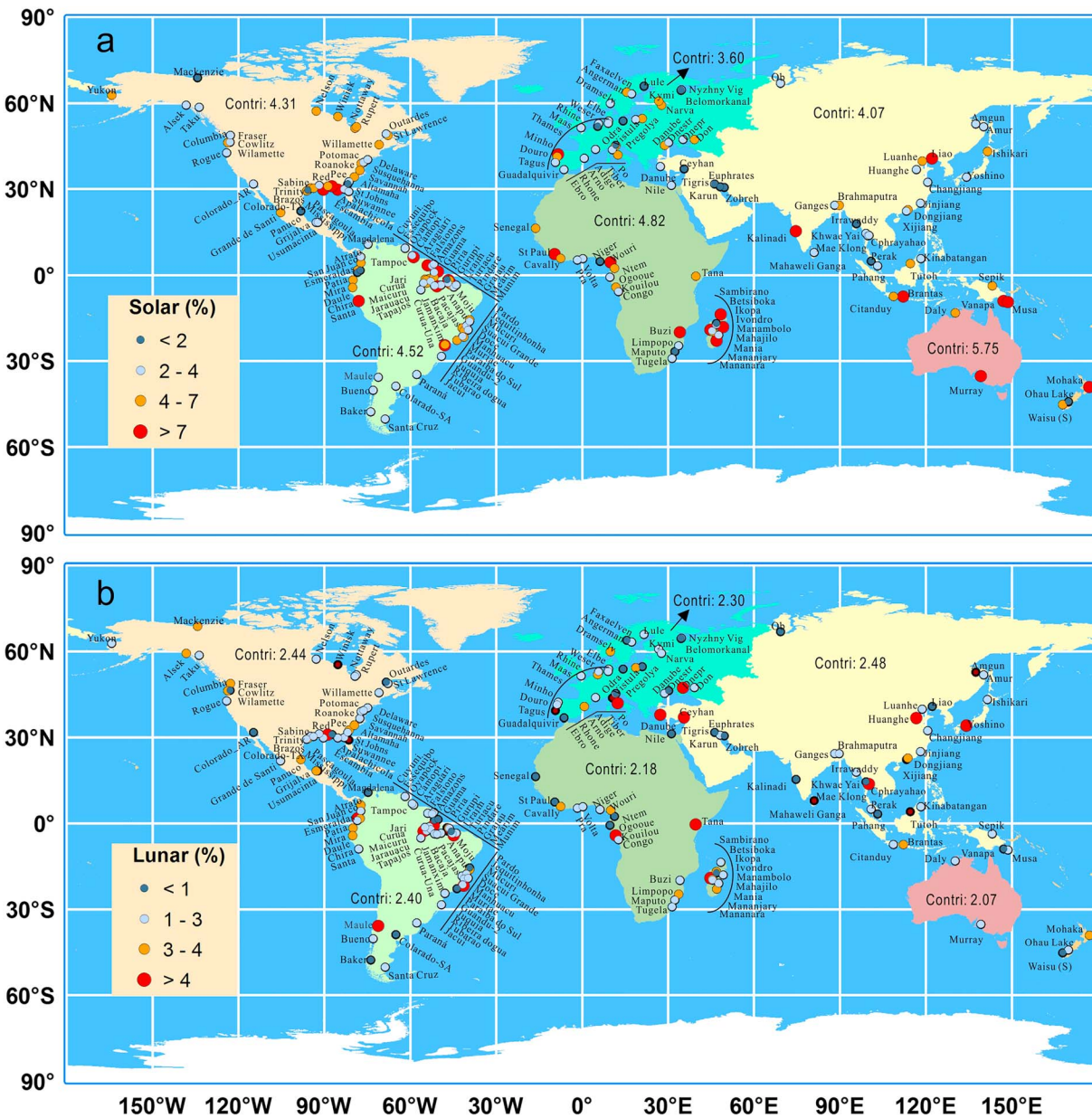
Figure 3. Impact of solar and lunar motion on the normalized river runoff ([a] contribution of solar motion; [b] contribution of lunar motion; Contri: the mean contributions of solar and lunar motions to the total river runoff for each continent, respectively).

3.2. The Impacts of SLPMs on Extreme Hydrological Events

It is already known that the effects of SLPMs can also be detected in the decadal climate variabilities (Agnihotri et al., 2002; Ray, 2007). Since rivers runoff is an excellent climatic indicator, stream flow is likely to be sensitive to changes in SLPMs (Mauas et al., 2011). Accordingly, a correlation analysis was performed between the number of sunspots and reconstructed stream flow fluctuations over an 11-year period for six rivers that are representative of six continents. We found that there is a strong synchronicity between the two variables at a significant level of 5% (Figure 4). Similar information between lunar declination angle and the reconstructed stream flow oscillations of 18–20 years can be also found with close relations at a significant level of 5% (Figure 5). In addition, it was determined that the extremely high or low values of the normalized runoff of most rivers correspond to crests or troughs or of the reconstructed runoff time series with fluctuation periods of 8.5~12 and 17~21.5 years, respectively (Figures 6a–6f and supporting information Figure S1). Moreover, the occurrence years of both the maximum number of sunspots and the maximum
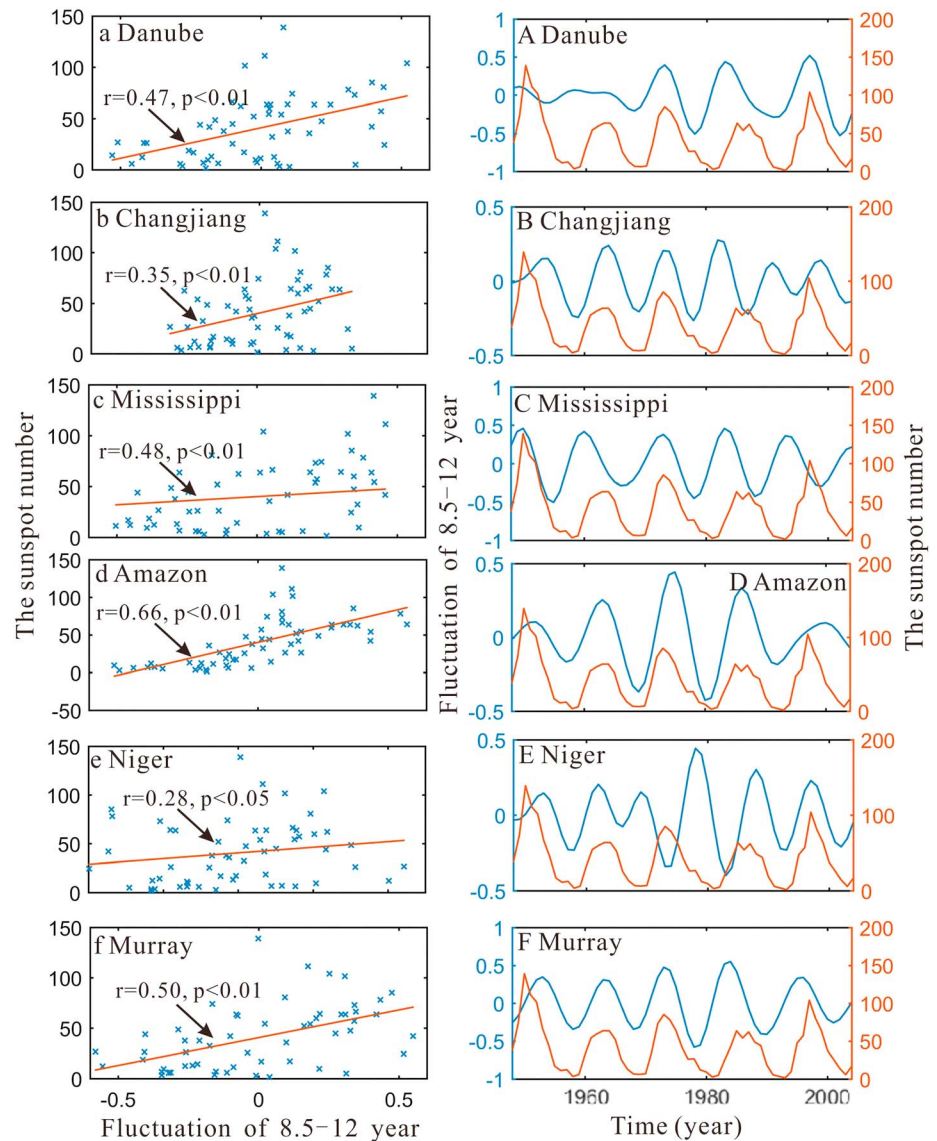
Figure 4. The reconstructed runoff fluctuation time series and the number of sunspots. r is the Pearson's correlation coefficient. However, r in Figure 4c is the lagged coefficient (lag time is one year). The figures in the left column (a–f) show the correlation analysis between sunspots and reconstructed runoff fluctuation, while that in the right column (A–F) exhibit the variation processes of sunspots and reconstructed runoff fluctuation.

lunar declination angle basically correspond to the crests of the reconstructed runoff time series with fluctuation periods of 8.5–12 and 17–21.5 years (Figures 6a–6f). There is also a good agreement between the occurrence years of both the minimum number of sunspots and the minimum lunar declination angle and the crests of the reconstructed runoff time series with fluctuation periods of 8.5–12 and 17–21.5 years (Figures 6a–6f). This finding indicates that the crests and troughs of SLPMs activity could diminish or enhance the runoff, which is in agreement with previous studies related to the stream flow of South American rivers (Mauas et al., 2008; Mauas et al., 2011). Moreover, if a longer time series of over 100 years of river discharge observations is taken into consideration, the calculated results for the discharge between 1879 and 2010 were in agreement with those for the discharge between 1948 and 2004, such as the case of the Columbia River (Figure 7). These findings imply that our results were not limited in river data time spans.
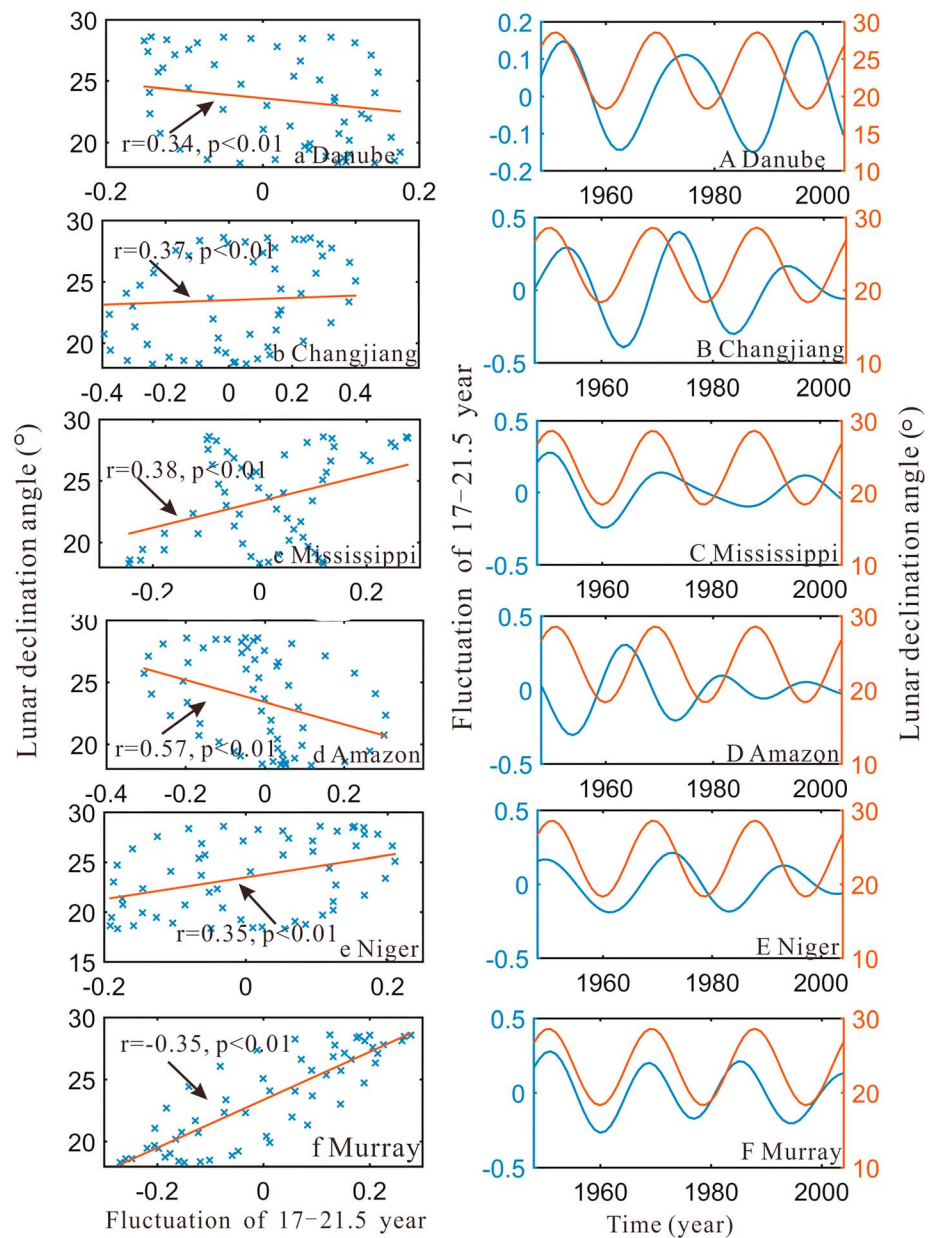
Figure 5. The reconstructed runoff fluctuation time series and the declination angle. r is the Pearson's correlation coefficient. However, *r* in Figures S1a and S1d is the lagged coefficient (lag time is 2 years). The figures in the left column (a–f) show the correlation analysis between sunspots and reconstructed runoff fluctuation, while that in the right column (A–F) exhibit the variation processes of sunspots and reconstructed runoff fluctuation.

We also examined the relationship between the occurrence of extreme droughts/floods in 190 rivers and the crests/troughs of the reconstructed runoff times with fluctuation periods of 8.5–12 and 17.5–21.5 years corresponding to SLPMs. There were 692 occurrences of extreme flood and 571 instances of extreme drought in the 190 rivers during the observed years of the study. The number of years of extreme flood events coinciding with SLPM crests was as high as 508. Similarly, the number of years of extreme droughts coinciding with SLPM crests was 483. There is close agreement between the occurrence of extreme droughts/floods in 190 rivers and the crests/troughs of the reconstructed runoff times with fluctuation periods of 8.5–12 and 17.5–21.5 years, respectively (supporting information Figure S1). In addition, the probability of extreme flood and drought years corresponding to SLPM peak and crest years was as large as 73% and 85%, respectively. This phenomenon is very similar to previous findings that indicate that various lunar oscillations
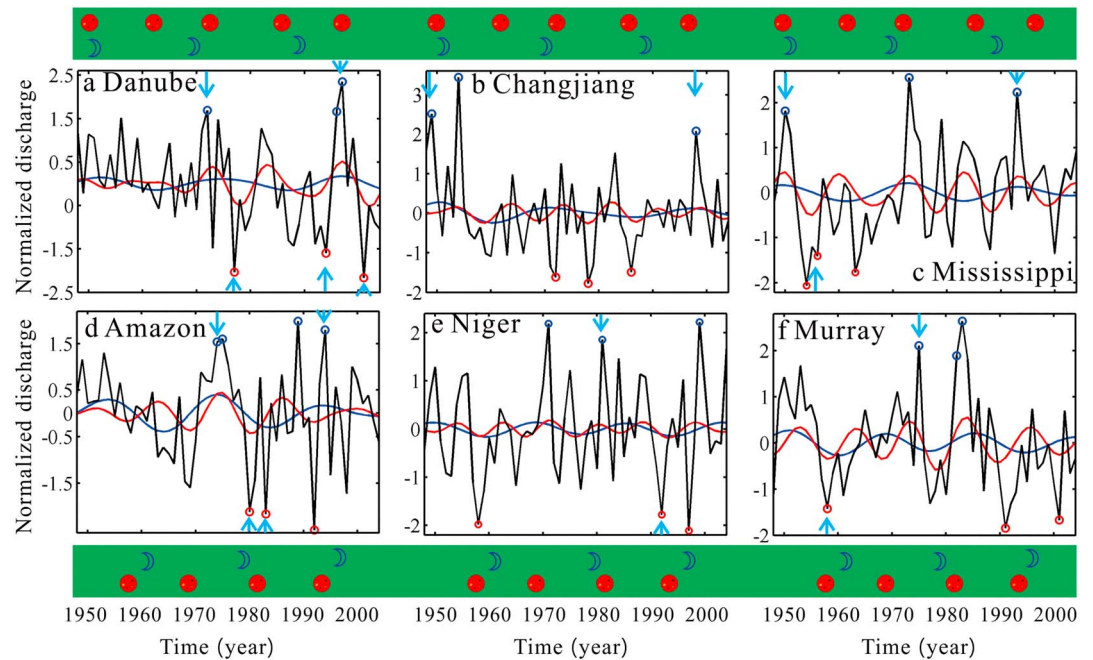
Figure 6. Changes in the normalized runoff and solar and lunar periodic motion cycles of typical rivers (Danube [a], Changjiang [b], Mississippi [c], Amazon [d], Niger [e], and Murray [f]); (black line: normalized runoff; red line: 8.5- to 12-year cycles; blue line: 17- to 21.5-year cycles. red circle: year of extreme drought; blue circle: year of extreme flooding. Locations of the top pictures of Sun and lunar: the times correspond to the occurrence year of the maximum number of sunspots and maximum lunar declination angle, respectively. Locations of the bottom pictures of Sun and lunar: the times correspond to occurrence year of the minimum number of sunspots and the minimum lunar declination angle, respectively).

can still produce storm flooding in coastal zones and/or significant erosion even if they only contribute approximately 3% of the variations in tidal amplitude (Gratiot, 2007). Moreover, a flood that occurred in approximately 1970 was observed to have been nearly synchronous in the European Danube River, the North American Mississippi River, and the African Niger River (Figures 6a, 6c, and 6e). We also observed that a drought that occurred in the Asian Changjiang River in approximately 1980 coincided with a drought that occurred in the South American Amazon River (Figures 4b and 4d). Most rivers of the world could experience synchronous floods and droughts in response to SLPMs such as the crests and troughs associated with solar activities in 1993 and 1997, respectively. Therefore, we speculate that the SLPMs could be an important factor impacting extreme flood and drought events and possibly magnifying the effects of SLPMs on runoff changes in most rivers in the world (Scafetta, 2010).

4. Discussion

The runoff of most rivers in the world has approximately quasi 2 years, 4- to 7-year, 8- to 12-year, and 17- to 21-year periods of frequency fluctuation, which could be affected by a very complex set of natural climatic variabilities (Agnihotri et al., 2002; Mauas et al., 2011). Internal climate variability or natural forcing (e.g., the Pacific Decadal Oscillation and the Atlantic Multidecadal Oscillation) is likely to be the direct driver of inducing oscillation of the rivers discharge. For example, both the Mississippi and Paraná rivers leveled off after 1997, perhaps in response to a subtle shift in the Pacific Decadal Oscillation (Figure 6c and supporting information Figure S1-No. 7; Dai et al., 2009).

The impacts of SLPMs on runoff changes should be not neglected even though their contributions to runoff changes are only 6.7%. While anthropogenic activities (e.g., dams and irrigation) have had broad impacts on rivers water discharge (Darby et al., 2016; Milliman et al., 2008), we found that the extreme high or low values of the normalized discharge of most rivers correspond well with SLPM crests or troughs, respectively (Figure 6 and supporting information Figure S1). For example, there was a relatively large flood in the Huanghe River after the Sanmenxia dam operation in 1960 (Wu et al., 2007) that corresponded to an
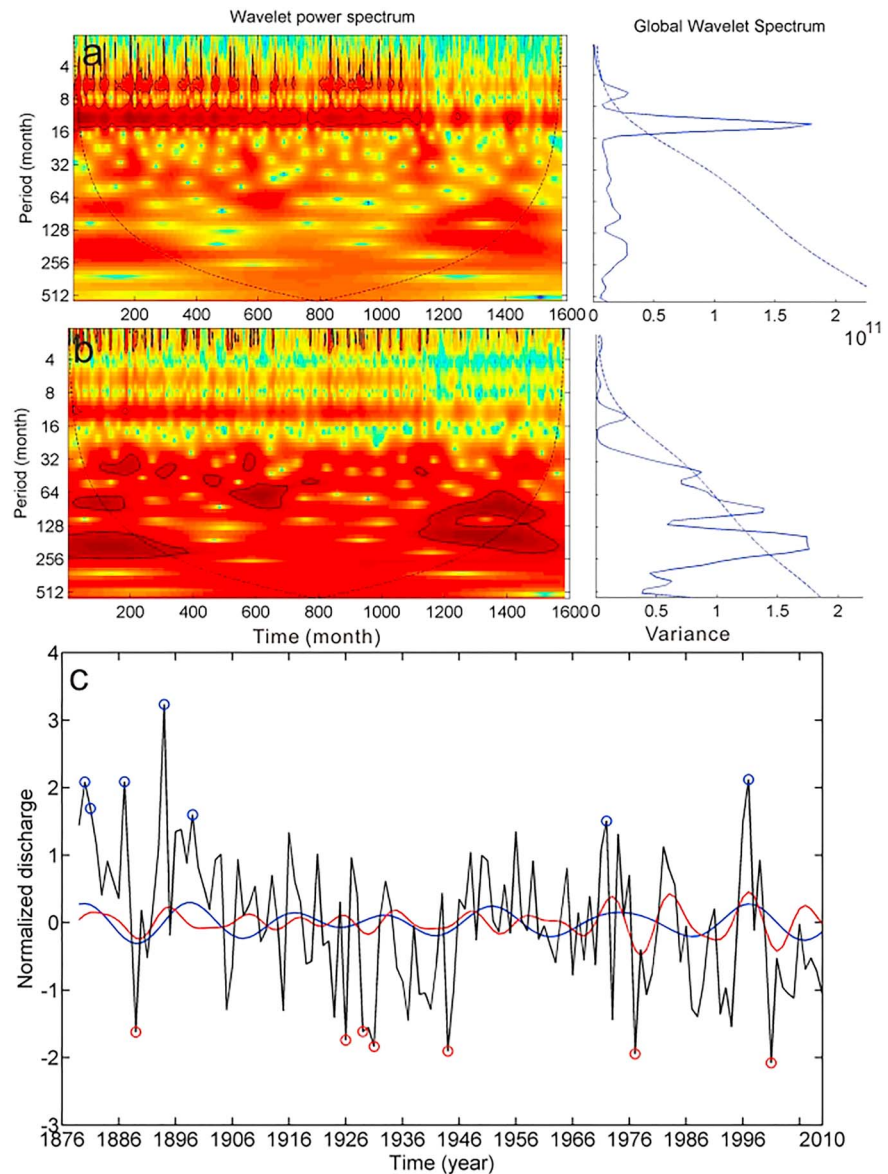
Figure 7. Changes in the normalized runoff of the Columbia River based on Morlet wavelet and global spectrum analysis ([a] original normalized runoff; [b] normalized runoff with filtered quasi-year fluctuations; [c] impact of solar and lunar periodic motions on the normalized river runoff [black line: normalized runoff; red line: 8.5- to 12-year cycles; blue line: 17- to 21.5-year cycles. red circle: year of extreme drought; blue circle: year of extreme flooding]).

SLPM crest (supporting information Figure S1-No. 34). Similarly, even though the Hoover Dam operation began in 1928 (Vano et al., 2012), the subsequent occurrence of extreme flood and drought years in the Colorado River basin agrees with maxima of SLPMs (supporting information Figure S1-No. 73). The recent research of White et al., 2005 indicated that Glen Canyon Dam affects the water discharge of the Colorado River at a short timescale on the basis of WA. Moreover, although European rivers have suffered from intense anthropogenic activities (Milliman et al., 2008), there are still related low contributions from SLPMs (Figure 3). In contrast, although the intensive human interferences have occurred on rivers in Australia, notable impacts from SLPMs are also detected (Figure 3). This indicates that the impact from SLPMs at multidecadal timescales could be unrelated to anthropogenic activities.

Moreover, the results related to the effects of SLPMs on river flows throughout the six continents considered in this study suggest that the influence of SLPMs is varied in different parts of the world (Figure 3). This could be induced by the difference in gravitational and magnetic forces in different geographical regions and the specific

local topographic properties of the rivers. In addition, climatic conditions at different latitudes cause enhanced solar activities, producing greater evaporation in relatively cloud-free regions in the subtropics; the resulting moisture then converges into the precipitation convergence zones (Mauas et al., 2008; Milliman et al., 2008). Hence, the distributed contribution feature along the latitude zone is in agreement with the impact of solar forces on the Earth's surface temperature and atmospheric circulation (Gray, 2003), which also coincides with precipitation distributions. For instance, large amounts of rainfall occurred at the equator and midlatitude, while low amounts of rainfall in subtropical zones (IPCC, 2007; Mauas et al., 2011).

5. Summary and Conclusions

Recently, extreme climate events (i.e., extreme floods and droughts) have occurred with increasing frequency (IPCC, 2007). Although most studies suggest that global warming has increased precipitation worldwide (Held & Soden, 2006; Huntington, 2006; Labat et al., 2004; Milly et al., 2005; Scafetta, 2010), our results demonstrate that the contribution of SLPMs to runoff is 6.7% on average. Our findings also show a significant correlation between occurrences of extreme floods and droughts and SLPM crests and troughs.

The current research tends to overlook the contribution of SLPMs to rivers runoff by primarily focusing on the anthropogenic impacts on hydrological variability (Held & Soden, 2006; Milly et al., 2005; Min et al., 2011), particularly for occurrences of extreme floods and droughts at a global scale. Our results show that SLPMs are one of the important factors in inducing anomalous events in global river runoff. There is an urgent need to conduct further research on this issue. The distribution feature of the contribution of SLPMs to the global runoff along the latitude zones should also have strong policy implications. This finding may increase the understanding of why extreme floods occur more frequently in tropical countries (e.g., Bangladesh) and why extreme droughts occur more frequently in the arid and semiarid regions of Africa (IPCC, 2007). SLPM fluctuations should receive more attention from policymakers, such as water resource managers, emergency managers, and hazard planners. In light of the impact of future climate change, SLPMs should be recognized as driving forces behind changes in river dynamics and accommodate anomalous runoff events into future climate mitigation and adaptation policies.

Appendix

The Appendix includes one table to support the main manuscript (Table A1).

Table A1
Characterization of River Gauging Stations With Location, Drainage Area, and the Mean Annual Runoff Records

River name	No.	Longitude	Latitude	Area[a] (km^2)	Vol[b] (km^3/year)	Station name	Country
Amazon	1	−51.75	−0.75	4,618,750	5,389.537	Obidos (Pcd)	BR
Congo	2	12.75	−5.75	3,475,000	1,270.203	Kinshasa	CD
Orinoco	3	−61.75	9.25	836,000	980.088	Puente Angostura	VE
Changjiang	4	120.75	32.25	1,705,383	905.141	Datong	CN
Brahmaputra	5	89.75	24.25	554,542	670.943	Bahadurabad	BD
Mississippi	6	−90.25	29.75	2,896,021	537.319	Vicksburg	US
Parana	7	−57.75	−34.75	2,346,000	476.584	Timbues	AR
Tapajos	8	−55.25	−2.75	387,378	337.803	Jatoba	BR
Ob	9	69.25	66.75	2,430,000	396.085	Salekhard	RU
Ganges	10	88.25	24.25	951,600	379.679	Farakka	IN
Irrawaddy	11	95.75	17.75	117,900	256.783	Sagaing	MM
St Lawrence	12	−67.75	48.75	1,344,200	224.654	Cornwall	CA
Amur	13	140.25	51.75	1,730,000	305.944	Komsomolsk	RU
Mackenzie	14	−134.25	68.75	1,660,000	283.431	Arctic Red River	CA
Xijiang	15	113.25	22.25	329,705	219.664	Wuzhou	CN
Columbia	16	−123.75	46.25	613,827	164.86	The Dalles	US
Magdalena	17	−74.75	10.75	257,438	230.904	Calamar	CO
Yukon	18	−164.25	62.75	831,386	227.464	Pilot	US
Atrato	19	−77.25	6.25	9,432	55.789	Tagachi	CO

Danube	20	28.75	45.25	807,000	203.739	Ceatal Izmail	RO
Niger	21	6.25	4.75	2,209,302.5	180.524	Lokoja	NGR
Ogooue	22	9.75	−0.75	203,500	147.964	Lambarene	GA
Essequibo	23	−58.75	6.25	66,600	66.436	Plantain Island	GY
Fraser	24	−122.75	48.75	217,000	85.43	Hope	CA
Nelson	25	−92.75	57.25	997,000	69.606	Bladder Rapids	CA
Sepik	26	143.25	−3.75	40,922	118.605	Ambunti	PG
Usumacinta	27	−92.25	18.25	50,743	58.594	Boca Del Cerro	MX
Rhine	28	5.75	52.75	180,000	70.459	Lobith	NL
San Juan co	29	−77.25	4.25	14,000	65.138	Penitas	CO
Tigris	30	46.25	31.75	134,000	38.193	Baghdad	IQ
Po	31	11.75	45.25	70,091	47.746	Pontelagoscuro	IT
Rhone	32	4.75	43.75	95,590	53.904	Beaucaire	FR
Dnepr	33	35.25	47.25	463,000	46.822	Dnepr	UA
Huanghe	34	116.75	36.75	734,146	44.924	Gaocun	CN
Jamanxim	35	−56.25	−5.25	40,400	37.088	Jamanxim	BR
Susquehanna	36	−76.25	39.25	62,419	30.392	Harrisburg	US
Don	37	39.25	47.25	378,000	24.447	Razdorskaya	RU
Santa Cruz	38	−68.75	−50.25	15,550	22.011	Charles Fuhr	AR
Oyapock	39	−51.75	3.75	25,100	26.381	Maripa	GF
Nile	40	31.25	31.25	2,900,000	39.571	El Ekhsase	EG
Nottaway	41	−77.41	50.01	57,500	32.542	Tete du Lac Soscumica	CA
Volta	42	0.25	5.75	394,100	33.918	Senchi (Halcrow)	GH
Willamette	43	−70.9	45.52	18,855	21.004	Salem	US
Red	44	−91.75	31.25	174,824	27.662	Alexandria	US
Pahang	45	103.25	3.25	19,000	16.895	Temerloh	MY
Chao Phraya	46	100.25	13.75	118,816	23.273	Wat Phikun Ngam	TH
Cuyuni	47	−59.25	6.75	53,400	35.671	Kamaria Falls	GY
Vistula	48	18.75	54.25	194,000	32.871	Tczew	PL
Rupert	49	−78.75	51.75	40,900	26.529	en Aval du Lac Nemiscau	CA
Esmeraldas	50	−78.25	1.75	18,800	31.726	D.J. Sade	EC
Doce	51	−39.75	−19.25	78,456	32.437	Linhares	BR
Jari	52	−53.25	−1.25	51,343	32.113	Sao Francisco (Pcd)	BR
Baker	53	−73.75	−47.75	23,736	27.443	La Colonia	CL
Araguari	54	−50.25	1.25	23,373	29.996	Porto Platon	BR
Douro	55	−8.75	41.25	91,491	17.317	Regua	PT
Kouilou	56	11.75	−4.25	55,010	28.584	Sounda	CG
Dongjiang	57	113.75	22.75	25,325	23.412	Boluo	CN
Elbe (Labe)	58	9.25	53.75	123,532	21.423	Wittenberge	DE
Alsek	59	−138.25	59.25	28,024	27.3	nr Yakutat	US
Paraiba do Sul	60	−41.25	−21.75	55,500	26.226	Campos-Ponte Municipal	BR
Karun	61	48.25	30.75	60,769	23.437	Ahvaz	IR
Kinabatangan	62	118.25	5.75	10,800	16.285	Balat	MY
Senegal	63	−16.25	16.25	268,000	21.691	Dagana	SN
Euphrates	64	46.25	31.75	274,100	19.149	Hindiya	IQ
Apalachicola	65	−85.25	29.75	44,548	19.987	Chattahoochee	US
Odra	66	14.25	53.75	109,729	16.724	Gozdowice	PL
Jequitinhonha	67	−39.25	−16.25	67,769	14.445	Itapebi	BR
Pánuco	68	−98.25	22.25	58,115	13.614	Las Adjuntas	MX
Limpopo	69	33.75	−24.75	342,000	11.677	Chokwe	MZ
Winisk	70	−85.25	55.25	50,000	13.304	Downstream Asheweig Tributary	CA
Ebro	71	0.75	40.75	84,230	14.82	Tortosa	ES
Narva	72	27.75	59.25	56,000	12.453	Narva Ges	EE
Colorado-AR	73	−114.75	31.75	444,701	12.36	Blw Hoover	US
Dniester	74	30.25	46.25	66,100	9.868	Bendery	MD
Tagus	75	−9.25	39.25	67,490	9.981	Almourol	PT
Murray	76	139.25	−35.25	991,000	8.518	Euston weir	VX
Grande de Santi	77	−105.25	21.75	128,943	8.375	El Capomal	MX
Brazos	78	−95.76	29.58	116,568	6.704	Richmond	US
Daly	79	130.25	−13.25	46,600	7.651	Mt Nancar	NT
Liao	80	122.25	40.75	120,764	3.512	Chiling	CN
Guadalquivir	81	−6.25	36.75	46,995	9.966	Alcala del Rio	ES

Colorado-TX	82	−96.1	29.31	108,787	2.583	Wharton	US
Grijalva	83	−92.75	18.25	37,702	16.92	Reforma	MX
Lule	84	21.67	65.8	24,707	15.811	Boden waterworks	SE
Mania	85	45.53	−19.8	17,990	15.499	Ankotrofotsy	MG
Amgun	86	137.5	52.7	41,000	15.224	Guga	RU
Gurupi	87	−46.32	−1.8	31,064	14.984	Alto bonito do Gurupi	BR
Ishikari	88	141.53	43.12	12,697	14.91	Ishikari-Ohashi	JP
Ribeira dogua	89	−47.84	−24.49	20,855	14.48	Registro 4F-002R	BR
Ikopa	90	46.85	−17.42	18,550	13.832	Antsatrana	MG
Mahajilo	91	45.47	−19.52	14,375	13.897	Miandrivazo	MG
Altamaha	92	−81.83	31.65	35,224	12.491	Doctortown	US
Outardes	93	−68.4	49.15	18,900	12.341	Centrale de Chute-aux- Outardes	CA
Taku	94	−133.7	58.54	16,896	12.247	nr Juneau	US
Bueno	95	−72.97	−40.32	3,714	12.231	Bueno	CL
Angerman	96	17.27	63.17	30,639	12.935	Solleftea	SE
Savannah	97	−81.26	32.53	25,511	10.779	Clyo	US
Delaware	98	−74.78	40.22	17,560	10.477	Trenton	US
Buzi	99	34.15	−19.95	26,314	10.516	Estaquinha	MZ
Maas (Meuse)	100	5.43	51.81	29,000	10.295	Lith	NL
Potomac	101	−77.13	38.95	29,940	10.211	Washington	US
Weser	102	9.13	52.97	37,788	9.981	Intschede	DE
Wouri	103	9.97	4.46	8,250	9.734	Yabassi	CM
Dramselv	104	9.92	59.9	16,020	9.703	Dovikfoss	NO
Daule	105	−80	−1.7	8,690	8.331	La Capilla	EC
Kymi	106	26.82	60.69	36,535	9.575	Pernoo	FI
Minho (Mino)	107	−8.38	42.08	15,457	7.878	Foz do Mouro	PT
Patía	108	−77.48	1.62	13,147	9.166	Pte Pusmeo	CO
Bacaja	109	−51.52	−3.77	23,070	9.169	Fazenda Cipauba	BR
Pascagoula	110	−88.72	30.98	17,068	9.028	Merrill	US
Pee Dee	111	−79.55	34.2	22,870	9.008	Pee Dee	US
Waiau (S)	112	167.8	−45.2	3,302	8.826	Lake Te Anau outflow	NZ
Ntem	113	11.3	2.3	18,100	8.697	Ngoazik	CM
Mae Klong	114	99.83	13.56	26,449	8.65	Ban Wang Khanai	TH
Betsiboka	115	46.93	−16.93	11,800	8.563	Ambodiroka	MG
Tutoh	116	114.64	3.97	3,210	8.364	Long Terawa	MY
Nyzhny Vig	117	34.67	64.48	26,600	8.27	Vigostrov	RU
Cowlitz	118	−122.91	46.28	5,796	8.237	Castle Rock	US
Musa	119	148.7	−9.35	4,210	8.267	Nadi Jabuna	PG
Belomorkanal	120	34.5	64.43	26,500	8.191	Matkozh	RU
Maule	121	−71.08	−35.7	5,454	7.75	Armerillo	CL
Mananara	122	46.97	−22.93	14,160	7.615	Maroangaty	MG
Sabine	123	−93.74	30.3	24,162	7.54	Ruliff	US
Roanoke	124	−77.63	36.46	21,720	7.341	Roanoke Rap	US
Adige (Etsch)	125	11.83	45.1	11,954	7.163	Boara Pisan	IT
Tiber (Tevere)	126	12.48	41.9	16,545	7.045	Ripetta (Roma)	IT
Ceyhan	127	35.63	36.97	20,466	7.022	Misis	TR
Trinity	128	−94.85	30.42	44,512	7.003	Romayor	US
St Paul	129	−9.53	7.33	9,760	6.735	Walker Bridge	LR
Mahaweli Ganga	130	81.1	7.92	7,343	6.501	Manampitiya	LK
Perak	131	100.97	4.82	7,770	7.016	Iskandar Bridge	MY
Suwannee	132	−82.93	29.96	20,409	6.309	Branford	US
Pindare	133	−45.46	−3.66	34,030	6.298	Pindare Mirim	BR
Pra	134	−1.63	5.17	22,714	6.216	Daboasi	GH
Juquia	135	−47.84	−24.38	5,390	4.134	Barranco Alto 4F-031	BR
Brantas	136	112.2	−7.48	8,650	5.815	Jabon	ID
Escambia	137	−87.23	30.97	9,886	5.683	Century	US
Cavally	138	−7.45	5.87	13,750	5.439	Tai	CI
Rogue	139	−124.06	42.58	10,202	5.348	Agness	US
Camopi	140	−52.35	3.17	5,920	5.271	Camopi	GF
Tana	141	39.67	−0.44	42,217	4.944	Garissa	KE
Mira	142	−78.47	0.87	4,960	4.547	d.j. Lita	EC
Guandu-2	143	−43.63	−22.82	1,353	4.629	Ponte do Guandu	BR
Faxaelven	144	15.64	63.84	6,432	4.603	Ulriksfors	SE

Santa	145	−78	−9	15,000	4.532	Pte Carretera	PE
Khwae Yai	146	99.12	14.43	10,880	4.431	Srinagarind Dam	TH
Tampoc	147	−53.83	3.42	7,650	4.504	Degrad-Roche	GF
Yoshino	148	134.2	34.05	2,768	4.907	Iwazu	JP
Vanapa	149	147.18	−9.05	1,940	4.384	Peto Island	PG
Sambirano	150	48.45	−13.68	2,980	4.315	Ambanja	MG
Guama	151	−47.1	−1.56	6,760	4.276	Bom Jardim	BR
Curua-Una	152	−54.27	−2.78	17,982	4.227	Jusante da Barragem-Conj1	BR
Moju	153	−49.21	−3.51	3,622	4.191	Cachoeira Tracambeua	BR
Colorado-SA	154	−64.95	−38.82	22,300	4.155	Pichi Mahuida	AR
Curua	155	−54.87	−1.5	20,803	4.122	Boca do Inferno	BR
Luanhe	156	118.75	39.72	44,100	4.129	Luanxian	CN
Falsino	157	−51.6	0.97	3,500	4.1	Ramos	BR
Pacajas	158	−50.63	−3.84	2,682	4.098	Pacajas	BR
Kalinadi	159	74.75	15.25	1,393	4.02	Dundeli	IN
Munim	160	−43.9	−3.46	12,350	3.993	Nina Rodrigues	BR
Manambolo	161	44.91	−19.14	1,893	3.842	Ambatolahy	MG
Maicuru	162	−54.4	−1.78	17,072	3.605	Arapari	BR
Mananjary	163	47.73	−21	2,260	3.57	Antsindra	MG
Mearim	164	−44.77	−4.22	25,500	3.377	Bacabal	BR
Ivondro	165	49.25	−18.18	2,545	3.367	Ringaringa	MG
Grajau	166	−45.22	−3.77	20,700	3.353	Aratoi Grande	BR
Mucuri	167	−40.35	−17.83	14,174	3.161	Nanuque	BR
Jarauacu	168	−52.8	−2.22	10,000	3.171	Fazenda Boa Esperanca	BR
Tugela	169	31.39	−29.14	28,920	2.798	Mandini	ZA
Bueyuek Mendere	170	27.4	37.76	23,889	3.11	Soeke	TR
Citanduy	171	108.72	−7.46	2,515	3.063	Cikawung	ID
Manhuacu	172	−41.16	−19.49	8,810	3.052	Sao Sebastiao da Encruzihada	BR
Maputo	173	32.43	−26.78	28,500	3.066	Madubula	MZ
Anapu	174	−51.37	−3.62	2,682	2.926	Fazenda Santo Antonio	BR
Muriae	175	−41.62	−21.49	7,270	2.881	Cardoso Moreira-Rv	BR
Arno	176	10.54	43.68	8,186	2.882	San Giovanni alla Vena	IT
Mohaka	177	177.13	−39.06	2,360	2.786	Raupunga	NZ
St Johns	178	−81.38	29.01	7,941	2.773	Deland	US
Suacui Grande	179	−41.92	−18.53	11,191	2.778	Vila Matias	BR
Pregolya	180	21.07	54.64	13,600	2.689	Gvardeysk	RU
Jinjiang	181	118.18	25.05	2,466	2.641	Anxi	CN
Chira	182	−80.15	−4.3	6,912	2.571	El Ciruelo	PE
Zohreh	183	49.67	30.5	12,600	2.573	Deh Molla	IR
Turiacu	184	−45.67	−2.94	3,762	2.525	Alto Turi	BR
Thames	185	−0.31	51.41	9,948	2.521	Kingston	UK
Piria	186	−46.59	−1.74	2,631	2.432	Tararua-Ponte	BR
Ohau Lake	187	169.83	−44.27	1,090	2.4	Lake Middleton	NZ
Uraim	188	−46.8	−2.77	4,668	2.172	Cafezal	BR
Tubarao	189	−49.11	−28.42	2,740	2.155	Rio do Pouso	BR
Pardo	190	−39.3	−15.57	29,138	2.439	Mascote	BR

[a]The controlled drainage area.   [b]The mean annual runoff.

References

Agnihotri, R., Dutta, K., Bhushan, R., & Somayajulu, B. L. K. (2002). Evidence for solar forcing on the Indian monsoon during the last millennium. *Earth and Planetary Science Letters*, *198*, 521–527.

Alexander, W. J. R., & Emeritus, W. J. R. (2005). Linkage between solar activity and climatic responses. *Energy and Environment*, *16*(2), 239–254.

Allen, M. R., & Ingram, W. J. (2002). Constraints on future changes in climate and the hydrologic cycle. *Nature*, *419*, 224–232.

Antico, A., & Kröhling, D. M. (2011). Solar motion and discharge of Paraná River, South America: evidence for a link. *Geophysical Research Letters*, *38*, L19401. https://doi.org/10.1029/2011GL048851

Briciu, A. E. (2014). Wavelet analysis of lunar semidiurnal tidal influence on selected inland rivers across the globe. *Scientific Reports-UK*, *4*, 4193. https://doi.org/10.1038/SREP04193

Brillinger, D. R. (1994). Trend analysis: Time series and point process problems. *Environmetrics*, *5*, 1–19.

Camuffo, D. (2001). *Lunar influences on climate. Earth, Moon and Planets* (Vol. 85, pp. 99–113).

Cerveny, R. S., Svoma, B. M., & Vose, R. S. (2010). Lunar tidal influence on inland river streamflow across the conterminous United States. *Geophysical Research Letters*, *37*, L22406. https://doi.org/10.1029/2010GL045564

Chou, C. (2013). Increase in the range between wet and dry season precipitation. *Nature Geoscience*, *6*, 263–267. https://doi.org/10.1038/ngeo1744

Coulibaly, P., & Burn, D. H. (2004). Wavelet analysis of variability in annual Canadian streamflows. *Water Resource Research*, *40*, W03105. https://doi.org/10.1029/2003WR002667

Currie, R. G., & Vines, R. G. (1996). Evidence for luni-solar Mn and solar cycle Sc signals in Australian rainfall data. *International Journal of Climatology*, *16*, 1243–1265.

Dai, A. G., Qian, T. T., Trenberth, K. E., & Milliman, J. D. (2009). Changes in continental freshwater discharge from 1948-2004. *Journal of Climate*, *22*, 2273–2292.

Dai, A. G., & Trenberth, K. E. (2002). Estimates of freshwater discharge from continents: latitudinal and seasonal variations. *Journal of Hydrometeorology*, *3*(6), 660–687.

Dai, Z. J., Liu, J. T., Wei, W., & Chen, J. Y. (2014). Detection of the Three Gorges dam influence on the Changjiang (Yangtze River) submerged delta. *Scientific Reports-UK*, *4*, 6600. https://doi.org/10.1038/srep06600

Darby, S. E., Hackney, C. R., Leyland, J., Kummu, M., Lauri, H., Parsons, D. R., et al. (2016). Fluvial sediment supply to a mega-delta reduced by shifting tropical-cyclone activity. *Nature*, *539*(7628), 276–279.

Gratiot, N. (2007). Significant contribution of the 18.6 year tidal cycle to regional coastal changes. *Nature Geoscience*, *1*, 169–172.

Gray, L. J. (2003). The influence of the equatorial upper stratosphere on stratospheric sudden warnings. *Geophysical Research Letters*, *30*(4), 1166. https://doi.org/10.1029/2002GL016430

Hajian, S., & Movahed, M. S. (2010). Multifractal detrended cross-correlation analysis of sunspot numbers and river flow fluctuation. *Phsica A*, *389*, 4942–4957.

Held, I. M., & Soden, B. J. (2006). Robust responses of the hydrological cycle to global warming. *Journal of Climate*, *19*, 5686–5699.

Hsu, K. C., & Li, S. T. (2010). Clustering spatial-temporal precipitation data using wavelet transform and self-organizing map neural network. *Advance in Water Resources*, *33*, 190–200.

Huntington, T. C. (2006). Evidence for intensification of the global water cycle: review and synthesis. *Journal of Hydrology*, *39*, 83–95.

Intergovernmental Panel on Climate Change (IPCC) (2007). In S. Solomon, et al. (Eds.), *Climate Change 2007: The Physical Science Basis—Contribution of Working Group I to the Fourth Assessment Report of the Intergovernmental Panel on Climate Change* (pp. 663–745). Cambridge Universe Press.

Kumar, P., & Foufoula-Georgiou, E. (1997). Wavelet analysis for geophysical applications. *Reviews of Geophysics*, *35*(4), 385–412.

Labat, D., Goddéris, Y., Probst, J. L., & Guyot, J. L. (2004). Evidence for global runoff increase related to climate warming. *Advance in Water Resources*, *27*, 631–642.

Lei, H. M., Yang, D. W., & Huang, M. Y. (2014). Impacts of climate change and vegetation dynamics on runoff in the mountainous region of the Haihe River basin in the past five decades. *Journal of Hydrology*, *511*, 786–799.

Lindsay, R. W., Percival, D. B., & Rothrock, D. A. (1996). The discrete wavelet transform and the scale analysis of the surface properties of sea ice. *IEEE Transactions on Geoscience and Remote Sensing*, *34*, 771–787.

Lindsay, S. D., & Farnsworth, R. K. (1997). Sources of solar radiation estimates and their effect on daily potential evaporation for use in streamflow modeling. *Journal of Hydrology*, *201*, 348–366.

Lu, X. X. (2004). Vulnerability of water discharge of large Chinese rivers to environmental changes: an overview. *Regional Environmental Change*, *4*(4), 182–191.

Mallat, S. A. (1989). *A wavelet tour of signal processing* (2nd ed., p. 637). San Diego: Academic Press.

Mauas, P. J. D., Buccino, A. P., & Flamenco, E. (2011). Long-term solar activity influences on South American rivers. *Journal of Atmospheric and Solar-Terrestrial Physics*, *198*, 521–527.

Mauas, P. J. D., Flamenco, F., & Buccino, A. P. (2008). Solar forcing of the stream flow of a continental scale South American river. *Physical Review Letters*, *101*.

Mei, X., Dai, Z., Darby, S., Gao, S., Wang, J., & Jiang, W. (2018). Modulation of extreme flood levels by impoundment significantly offset by floodplain loss downstream of the Three Gorges Dam. *Geophysical Research Letters*, *45*, 3147–3155. https://doi.org/10.1002/2017GL076935

Milliman, J. D., Farnsworth, K. L., Jones, P. D., Xu, K. H., & Smith, L. C. (2008). Climatic and anthropogenic factors affecting river discharge to the global ocean, 1951–2000. *Global Planet Change*, *62*, 187–194.

Milly, P. C. D., Dunne, K. A., & Vecchia, A. V. (2005). Global pattern of trends in stream flow and water availability in a changing climate. *Nature*, *438*(17), 347–350.

Min, S. K., Zhang, X. B., Zwiers, F. W., & Hgerl, G. C. (2011). Human contribution to more-intense precipitation extremes. *Nature*, *17*, 378–381.

Mishali, M., & Eldar, Y. C. (2010). From theory to practice: Sub-Nyquist sampling of sparse wideband analog signals. *IEEE Journal of Selected Topics in Signal Processing*, *4*(2), 375–391.

Mount, N. J., Tate, N. J., & Sarker, M. H. (2013). Evolutionary, multi-scale analysis of river bank line retreat using continuous wavelet transforms: Jamuna river, Bangladesh. *Geomorphology*, *183*, 82–95.

North, G. R., & Stevens, M. J. (1998). Detecting climate signals in the surface temperature record. *Journal of Climate*, *11*(4), 563–577.

Percival, D. B. (1995). On estimation of the wavelet variance. *Biometrika*, *82*, 619–631.

Prokoph, A., Adamowski, J., & Adamowski, K. (2012). Influence of the 11 year solar cycle on annual streamflow maxima in Southern Canada. *Journal of Hydrology*, *442*, 55–62.

Ray, D. R. (2007). Decadal climate variability: is there a tidal connection? *Journal of Climate*, *20*, 3542–3560.

Rind, D. (2002). The Sun's role in climate variations. *Science*, *296*, 673–677.

Sadowsky, J. (1996). Investigation of signal characteristics using the continuous wavelet transform. *Johns Hopkins APL Technical Digest*, *17*, 258–269.

Scafetta, N. (2010). Empirical evidence for a celestial origin of the climate oscillations. *Journal of Atmospheric and Solar-Terrestrial Physics*, *72*, 951–970.

Scafetta, N. (2013). Discussion on climate oscillations: CMIP5 general circulation models versus a semi-empirical harmonic model based on astronomical cycles. *Earth-Science Reviews*, *126*, 321–357.

Seleshi, Y., Demaree, G. R., & Delleur, J. W. (1994). Sunspot numbers as a possible indicator of annual rainfall at Addis Ababa, Ethiopia. *International Journal of Climatology*, *14*(8), 911–923.

Tang, Q. H., & Lettenmaier, D. P. (2012). 21st century runoff sensitivities of major global river basins. *Geophysical Research Letters*, *39*, L06403. https://doi.org/10.1029/2011GL050834

Timoney, K., Peterson, G., Fargey, P., Peterson, M., McCanny, S., & Wein, R. (1997). Spring ice-jam flooding of the Peace-Athabasca delta: Evidence of a climatic oscillation. *Climatic change*, *35*, 463–483.

Torrence, C., & Compo, G. P. (1998). A practical guide to wavelet analysis. *Bulletin American Meteorological Society*, *9*, 61–78.

Vano, J. A., Das, T., & Lettenmaier, D. P. (2012). Hydrologic sensitivities of Colorado River runoff to changes in precipitation and temperature. *Journal of Hydrometeorology*, *13*, 932–949.

White, M. A., Schmidt, J. C., & Topping, D. J. (2005). Application of wavelet analysis for monitoring the hydrologic effects of dam operation: glen canyon dam and the Colorado River at Lees ferry, Arizona. *River Research Application*, *21*, 551–565.

Wu, B. S., Wang, G. Q., & Xia, J. Q. (2007). Delayed sedimentation response to inflow and operations at Sanmenxia Dam. *Journal of Hydraulic Engineering*, *133*(5), 482–494.

Zhang, Q., Jiang, T., Chen, Y. Q., & Chen, X. H. (2010). Changing properties of hydrological extremes in south China: Natural variations or human influences? *Hydrological Processes*, *24*(11), 1421–1432.

Zhang, Q., Sun, P., Jiang, T., Tu, X. J., & Chen, X. H. (2011). Spatio-temporal patterns of hydrological processes and their hydrological responses to human activities in the Poyang Lake basin, China. *Hydrological Sciences Journal*, *56*(2), 305–318.